FULL PAPER

In orbit calibration of the non-orthogonality of the two fluxgate sensors onboard CSES

Yuqi Tong[1,2,3], Bin Zhou[1,2]*, Lei Li[1,2], Bingjun Cheng[1,2], Yiteng Zhang[1,2], Werner Magnes[4], Roland Lammegger[5], Andreas Pollinger[4], Yanyan Yang[6], Zhima Zeren[6] and Xuhui Shen[6]

Abstract

With the accumulation of data, it is possible to study the long-term variation of Fluxgate Magnetometers (FGM) of High Precision Magnetometer (HPM) onboard the China Seismo-Electromagnetic Satellite (CSES). The calibration method of HPM depends on an assumption that the linear parameters of FGM, including the gain factors, the offsets, and non-orthogonal angles are stable. However, HPM exhibits some unexpected trends in the scalar residuals when processed according to the assumption. Study on the residual finds out that under changing space thermal conditions, the non-orthogonal angles of FGM change periodically, suggesting that the data calibration method we used before should be modified. A multi-dimensional polynomial model is established for defining the change of non-orthogonal angles of FGM as a function of the sun incidence angles, geographic latitude and sensor temperature. Apply the polynomial model to data from August 2018 to May 2021, the standard deviation of the scalar residuals is reduced to around 0.5 nT and tends to be more random and in line with the normal distribution. Meanwhile, the variation trend in gain factors and offset factors are eliminated. Results show that the model can correctly reflect the period variation of the non-orthogonal angles of FGM with the space thermal conditions.

Keywords High precision magnetometer, Fluxgate magnetometer, Instrument calibration, CSES satellite
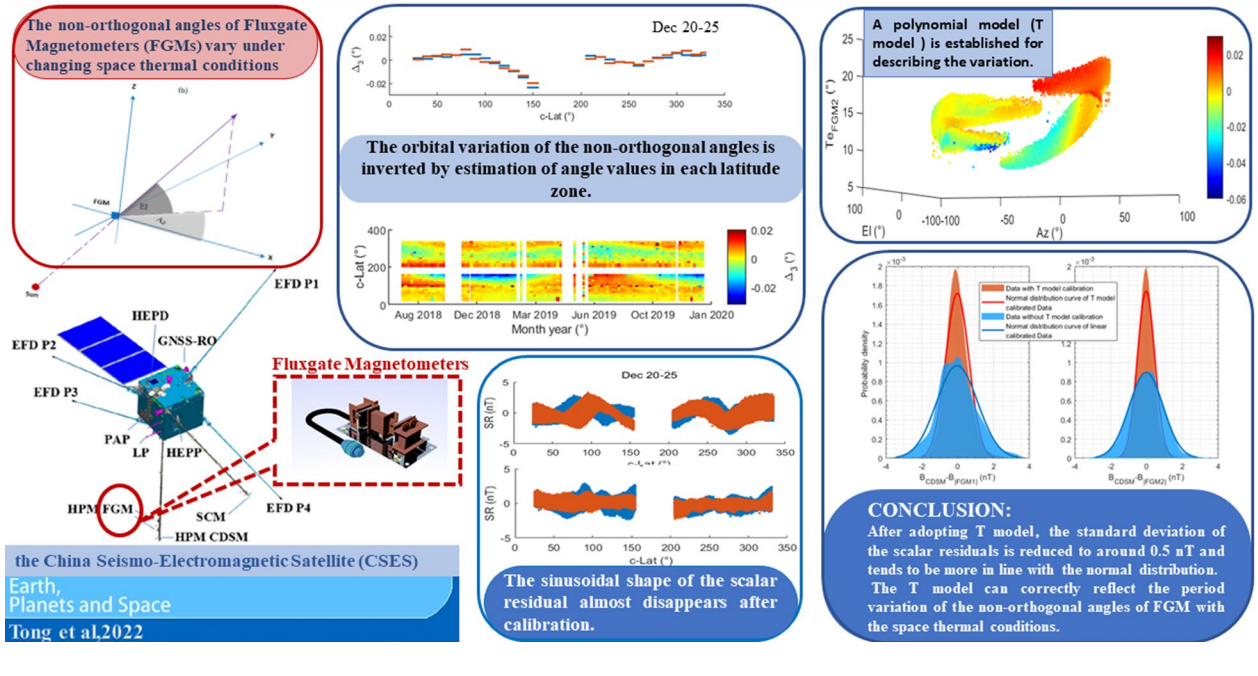
*Correspondence:
Bin Zhou
zhoubin@nssc.ac.cn
Full list of author information is available at the end of the article

Tong *et al. Earth, Planets and Space*   (2023) 75:21

Page 2 of 15

Graphical Abstract

Introduction

China Seismo-Electromagnetic Satellite (CSES), also named ZHANGHENG-1, was launched on February 2, 2018, to measure the geophysical fields and ionospheric disturbances related to the earthquakes. CSES operates on a sun-synchronous circular orbit with an initial altitude of 507 km and an inclination of 97.4°, and it has a descending local time at 14:00 and a 5 day revisiting period (Shen et al. 2018). CSES has eight scientific payloads, among which the High Precision Magnetometer (HPM), composed of two types of sensors, Fluxgate Magnetometers (FGM1 and FGM2) (Cheng et al. 2018) and a scalar magnetometer named Coupled Dark State Magnetometer (CDSM) (Pollinger et al. 2018), can measure the geomagnetic field from DC to 15 Hz. Zhou et al. (2018) introduced the HPM data processing method in detail from four aspects: ground sensor correction, in-orbit linear calibration, satellite interference elimination, and coordinate system transformation. During the process of in-orbit calibration, it is assumed that the parameters of the vector sensor are stable and do not change. Tong et al. (2021) explained the interference mechanism between tri-band beacon (TBB) and FGM and presented an interference elimination solution for FGM vector data. Zhima et al. (2022) confirmed the good consistency between HPM and Search Coil Magnetometer onboard CSES in the ultra-low-frequency (ULF) range using the magnetic torque (MT) signal source as a reference. Nearly, 4 years of continuous operation proves that HPM has excellent performance in-orbit, and the HPM data maintain long-term stability and high-quality, and keep consistent with the magnetic field data of Swarm constellation (Zhou et al. 2019; Pollinger et al. 2020; Yang et al. 2021a, b; Zhang et al. 2022).

The configuration design, performance and data processing of HPM enable it to produce high-quality vector magnetic field data in orbit, which support the geomagnetic field modeling (Yang et al. 2021a, b; Wang et al. 2021). However, coupling of the complex satellite platform and space environment may have some mixed and long-lasting effects on magnetic field detection. For example, the offsets of vector magnetometer onboard Oersted changed due to atmospheric pressure stress relief and mechanical stress changes (Primdahl et al. 2006); The temporal variation of the gain factors of the FGM on CHAMP was logarithmically fitted, which was probably related to aging of the electronic devices, e.g., radiation effects (Yin and Lühr 2011); The magnetic field vector disturbances on all three Swarm spacecrafts, which may be related to thermal capacitance and the

Tong *et al. Earth, Planets and Space*   (2023) 75:21

Page 3 of 15

direction to the Sun (Tøffner-Clausen et al. 2016). The above problems were calibrated by specific scalar equation methods according to the detailed study of the characteristics of satellite platform and space environment. As the first electromagnetic satellite of China, CSES carried out a full set of magnetic cleanness designs and tests, but neither had a stability design adopting special optical bench, nor a constant temperature sensor design. Lacking of special designs for magnetic field detection, combined with the low-earth orbit space environment, may have a long-term impact on the FGM sensor parameters.

This paper will describe the trends in scalar residuals and phenomena in FGM data after preliminary linear calibration based on CDSM scalar magnetic field data. We study the changes of FGM non-orthogonal angles at different geographic latitudes and their long-term variation. A model describing both orbital variation and annual variation of orthogonal angle based on Taylor polynomials will be developed. Data calibration results, evaluation and verification will be presented.

Characteristics of calibration data in orbit

Low-earth orbit magnetic mapping missions (Magsat, Oersted, CHAMP, SAC-C MMP and Swarm) typically have similar configurations. They all carry a vector magnetometer and a scalar magnetometer which is used as magnetic reference to calibrate instrument parameters of the vector magnetometer, including the gain factors, the offsets, and non-orthogonal angles (Langel et al. 1982; Olsen et al. 2003; Rother et al. 2005; Friis-Christensen et al. 2006). As CDSM and FGM synchronously and independently measure the background magnetic field onboard CSES, theoretically the strength of magnetic field from both CDSM and FGM should agree with each other. According to the scalar equation $B_{CDSM} = |\mathbf{B}_{FGM}|$, $|\mathbf{B}_{FGM}|$ is the modulus of the FGM vector magnetic field data, and B_{CDSM} is the magnetic intensity measured by the CDSM, the scalar residual, $B_{CDSM} - |\mathbf{B}_{FGM}|$, should maintain a small value close to zero after linear calibration of FGM data. However, in fact it is not the case. One revisit cycle of the magnetic field data is selected every month in 2019, and calibrated by the linear calibration method proposed by Zhou (Zhou et al. 2018). Circle latitude (c-Lat) is defined, as shown in Fig. 1, where the abscissa is 180°-colatitude for ascending, and 180°+colatitude for the descending orbit, the scalar residuals of FGM1 (blue dot) and FGM2 (red dot) magnetic field data are anti-phased sinusoidal distributions along the ascending orbit, while in-phase along the descending orbit, with peak values as large as several nT. Moreover, the shape and the amplitude of the residuals in January are almost similar to that in December. During the initial stage of CSES in orbit, Zhou et al. (2019) found that the FGM linear parameters on the dayside
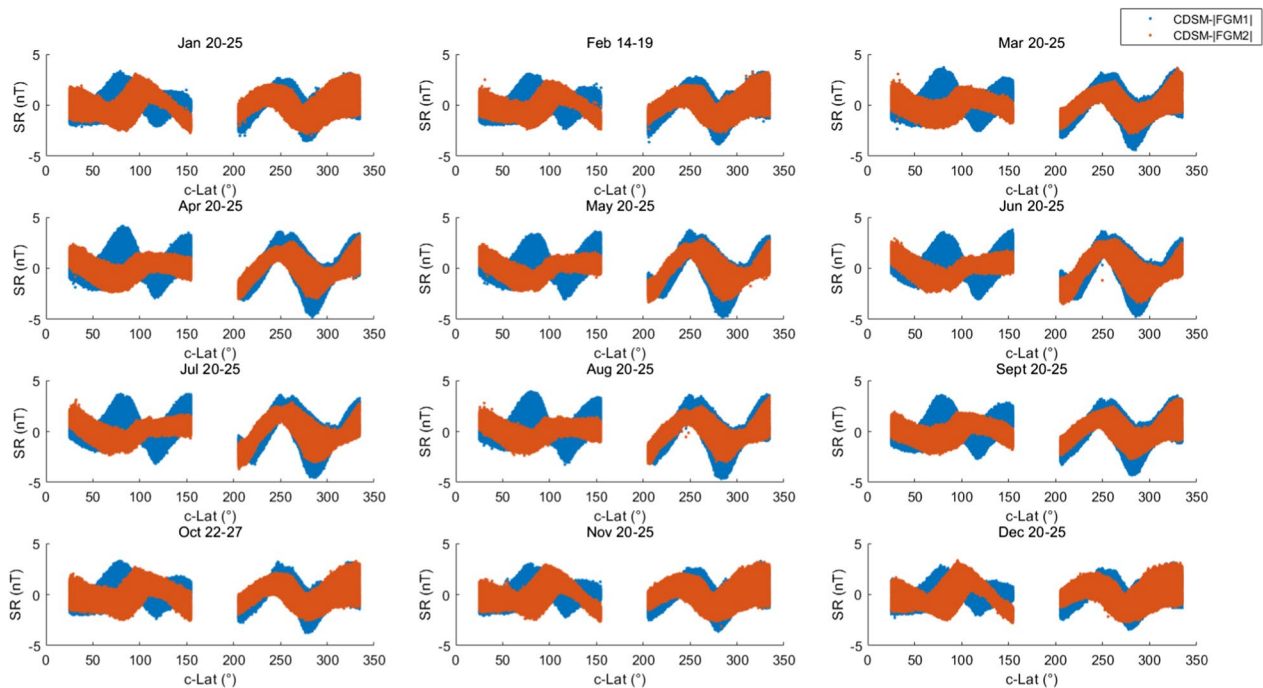

Fig. 1 The scalar residuals (SR) of magnetic field data after linear calibration, FGM1 (blue dot) and FGM2 (red dot) data selected in one revisit cycle every month in 2019 are shown in the geographical coordinate system

Tong *et al. Earth, Planets and Space*   (2023) 75:21

Page 4 of 15

were different from that on the nightside, and to reduce the fitting residual of the data, they processed the dayside and nightside magnetic field data separately every day. The fitting residual was apparently reduced, but the fitting was based on data covering only one hemisphere, which brought some fitting errors in FGM linear parameters. Meanwhile, the discontinuity in linear parameters between dayside and nightside could not be explained.

The extreme in scalar residuals happen when the Y and Z components of the vector magnetic field in the FGM orthogonal coordinate system are approximately equal. This phenomenon can be directly analyzed with the help of a two-dimensional model [Eqs. (1), (2), (3)], because the measured X component of the magnetic field is much weaker than the Y and Z components. The extreme scalar residuals will appear around magnetic inclination of 45°, where small non-orthogonality exists. As can be evaluated from Eqs. (1), (2), (3), where α is the inclination angle between the magnetic field and Y (y) axis, θ is the non-orthogonal angle between the orthogonal axis Z and the non-orthogonal axis z, when the small non-orthogonal angle θ exists and the scalar magnetic field B_S is stable, the extreme values of ΔB_S will appear at $\alpha = 45°$. In

and the drift caused by temperature was corrected before in orbit data processing (Zhou et al. 2018). However, we did not test the thermal drift of non-orthogonal angles on the ground, since the orthogonality is affected by the installation conditions which are different in orbit. Therefore, the orthogonality variation of vector magnetometer should be the main cause of the trends in scalar residuals at present. We, therefore, hypothesize that the influence of non-orthogonal angles is the dominant cause, since gains and offsets have already been corrected according to the ground calibrations. Consequences of this hypnosis will be discussed at the end of the paper.

Inversion of non-orthogonal angle variations

The scalar residuals have a fixed pattern (see Fig. 1), but it is difficult to directly invert the specific variations of non-orthogonal angles in orbit from them. Therefore, we use differentiation method to deal with this problem. Figure 2 shows the definition of three non-orthogonal angles ($\theta_1, \theta_2, \theta_3$). The matrix **M** transforms the magnetic field vector from orthogonal coordinate system (X,Y,Z) to non-orthogonal coordinate system (x,y,z), and

$$M(\theta_1, \theta_2, \theta_3) = \begin{pmatrix} 1 & 0 & 0 \\ \sin(\theta_1) & \cos(\theta_1) & 0 \\ \sin(\theta_2) & \sin(\theta_3) & \sqrt{1 - \sin(\theta_2)^2 - \sin(\theta_3)^2} \end{pmatrix} \tag{4}$$

fact, B_S constantly varies and θ may also constantly vary in orbit, so the extreme values of ΔB_S will appear near $\alpha = 45°$. This indicates the most likely scenario in orbit, that the non-orthogonal angles constantly vary in orbit and, therefore, deviate from their average values set by the scalar calibration. Equation (3) can also explain the antiphase or in-phase phenomenon of FGM1 and FGM2 scalar residuals in Fig. 1, which may be related to the phase of the non-orthogonal angle variations:

$$\begin{bmatrix} 1 & 0 \\ \sin \theta & \cos \theta \end{bmatrix} \begin{bmatrix} B_Y \\ B_Z \end{bmatrix} = \begin{bmatrix} B_y \\ B_z \end{bmatrix}, \tag{1}$$

$$B_Y = \cos \alpha B_S, B_Z = \sin \alpha B_S, \tag{2}$$

$$\Delta B_S = \sqrt{B_Y^2 + B_Z^2} - B_S \sin \theta \sin (2\alpha), \tag{3}$$

The strict magnetic cleanliness measures had been taken for the CSES, the uncertainty of magnetic field interference reaches < 0.3 nT at the end of the HPM boom (Qi et al. 2018). The thermal drift of offsets and gains were fully tested on the ground (Cheng et al. 2018),

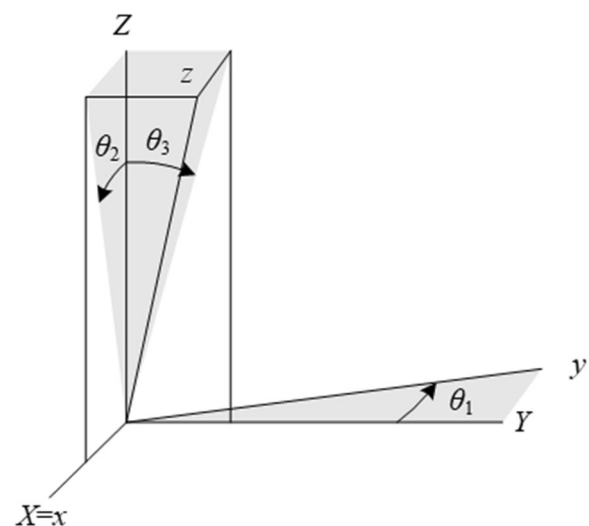As shown in Fig. 3, according to the distribution of scalar residuals versus latitude, the spherical surface is

Fig. 2 The definition of three non-orthogonal angles in the FGM sensor coordinates. The orthogonal coordinate is represented by the capital letters X, Y, Z; and the non-orthogonal coordinate is denoted by the lower-case x, y, z
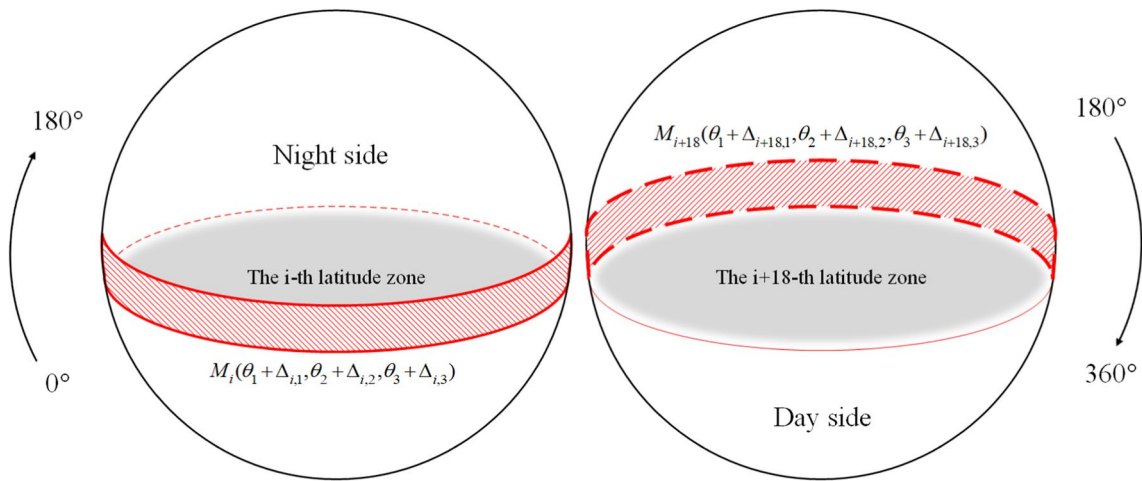
Fig .3 The relationship between latitude zones and non-orthogonal angle matrixes, the matrix of the ith latitude zone is $M_i\left(\theta_1 + \Delta_{i,1}, \theta_2 + \Delta_{i,2}, \theta_3 + \Delta_{i,3}\right)$

divided into different zones latitudinally, assuming that the non-orthogonal angles are constant in one latitude zone. The orbital variation of the non-orthogonal angles in orbit is inverted by estimation of angle values in each zone. Theoretically, the more latitude zones, the more details of orbital variation, but at the same time greater random error. The width of latitude zones is tested from 1° to 30°, and results show that the scalar residuals are significantly improved when the latitude zones have a width of 10°, and the orbital variation of the non-orthogonal angles are also well-reflected. Therefore, the relationship between FGM output B_x, B_y, B_z and the ambient vector magnetic field B_X, B_Y, B_Z changes from Eqs. (5) to (6):

$$\begin{bmatrix} B_X \\ B_Y \\ B_Z \end{bmatrix} = M^{-1}(\theta_1, \theta_2, \theta_3) \begin{bmatrix} a_x(B_x + b_x) \\ a_y(B_y + b_y) \\ a_z(B_z + b_z) \end{bmatrix}, \qquad (5)$$

$$\begin{bmatrix} B_X \\ B_Y \\ B_Z \end{bmatrix} = \begin{cases} M_1^{-1}\left(\theta_1 + \Delta_{1,1}, \theta_2 + \Delta_{1,2}, \theta_3 + \Delta_{1,3}\right) \begin{bmatrix} a_x(B_x + b_x) \\ a_y(B_y + b_y) \\ a_z(B_z + b_z) \end{bmatrix}, 0 \le lat < 10 \\ \dots \\ M_i^{-1}\left(\theta_1 + \Delta_{i,1}, \theta_2 + \Delta_{i,2}, \theta_3 + \Delta_{i,3}\right) \begin{bmatrix} a_x(B_x + b_x) \\ a_y(B_y + b_y) \\ a_z(B_z + b_z) \end{bmatrix}, 10*(i-1) \le lat < 10*i \\ \dots \end{cases}, \qquad (6)$$

where i is the index of latitude zone, $i = 1$ to 36; a_x, a_y, a_z and b_x, b_y, b_z are the gain factors and offsets of the three components for the full orbit, respectively. The objective function is established based on the scalar equation as follows:

$$L(\mathbf{m}) = \sum_{k=1}^{n} (B_{CDSM_k} - \sqrt{B_{X_k}^2 + B_{Y_k}^2 + B_{Z_k}^2})^2, \qquad (7)$$

where k indexes magnetic field data in chronological order and n is the total data number in a revisit cycle. The objective function $L(\mathbf{m})$ is a piecewise function containing 9 global parameters $(a_{x,y,z}, b_{x,y,z}, \theta_{1,2,3})$ plus $108 = 3 * 36$ local parameters $(\Delta_{i,1,2,3})$, $\mathbf{m} = (a_x, a_y, a_z, b_x, b_y, b_z, \theta_1, \theta_2, \theta_3, \Delta_{1,1}, \Delta_{1,2}, \Delta_{1,3}\dots\dots,)$ $(\Delta_{36,1}, \Delta_{36,2}, \Delta_{36,3})$, (total number of parameters: $D = 9 + 108$).

Particle swarm optimization (PSO) (Kennedy 2011; Mezura-Montes and Coello 2011; Pedersen 2010) is introduced to optimize the objective function. Compared with the classic optimization methods, such as gradient descent and Newton or quasi-newton methods, PSO does not require the objective function to be differentiable. Set the boundary conditions and initialize N particles, the position of the jth particle is $\mathbf{m}_j, j = 1, 2, 3, \dots, N$, and its dth

Tong *et al. Earth, Planets and Space* (2023) 75:21

Page 6 of 15

dimension is m_{jd}, $d = 1, 2, 3, ..., D$, $d = 1$ represents the gain of the X component, and so on. Initialize the particle position m_{jd}^0 and velocity v_{jd}^0. Then, the position and velocity of particle are updated by two extreme values. $p_{jd}^t(p_{jd}^0 = m_{jd}^0)$ is the best position achieved by jth particle so far. Choose a random subset S among N particles except jth particle, p_{gd}^t is the best position obtained by subset S so far. The tth iteration of the jth particle in dth dimension is obtained by the following equations:

$$v_{jd}^{t+1} = wv_{jd}^t + \left(p_{jd}^t - m_{jd}^t\right) + c_2 r_2 \left(p_{gd}^t\_m_{jd}^t\right), \quad (8)$$

$$m_{jd}^{t+1} = m_{jd}^t + v_{jd}^{t+1}, \quad (9)$$

where w is the dynamic inertia weight, c1 and c2 are fixed learning factors with values of 1.5, $r1$ and $r2$ are random variables with uniform distribution in [0,1]. The swarm particles move toward the best solutions under the relative influence of the previous velocity vector, self-cognitive and social component until the relative change of $L(p_g)$ converges.

We interpolate the optimal value of Δ along latitude by cubic spline, and calibrate the magnetic field data in Fig. 1. As shown in Fig. 4, the scalar residuals of FGM1 (blue dot) and FGM2 (red dot) reduced significantly after the variation of the non-orthogonal angles is considered, and the sinusoidal shape of the scalar residual

almost disappears. In addition, a weak annual variation in the non-orthogonal angles is found when calculating Δ with more revisit cycles as shown in Fig. 5 (data with interferences from TBB and magnetic torque have been removed): Δ_1 does not have obvious variation pattern in-orbit; Δ_2 has a large random error at high latitudes; while Δ_3 has an obvious seasonal variation. This may be due to the fact that CSES operates in a three-axis stabilized platform. The x-component of the sensor, which is perpendicular to the orbital plane (east–west direction), measures weaker geomagnetic field, and leads to larger errors in Δ_1 and Δ_2. Figure 6 takes December 20–25 as an example, the Δ value of the FGM2 exhibits substantial similarity in 2018 and 2019, which is most obvious in Δ_3. Overall, Δ gradually changes throughout the year but is almost identical on the same day in different years. Therefore, we infer that, Δ has an annual variation.

Non-orthogonal angle annual variation model

We can analyze the possible reasons for the annual variation of Δ in terms of the complex external thermal flow of CSES in space. The solar illumination (see Fig. 7) is represented by the solar incident angles in the orthogonal coordinate system (X,Y,Z), the azimuth (Az, $-180° \sim 180°$) and elevation (El, $-90° \sim 90°$) of the solar vector are shown in Fig. 7b. The earth albedo is complex, not only has seasonal and diurnal
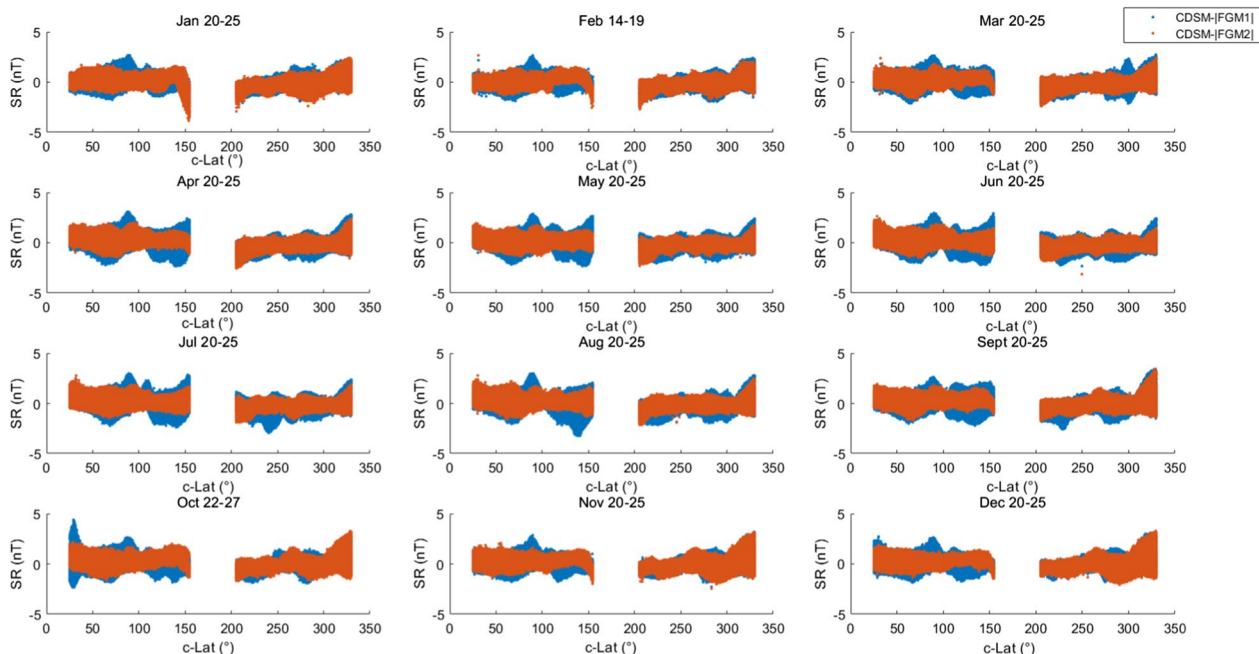

Fig. 4 The scalar residuals (SR) of magnetic field data after the variation in the non-orthogonal angles are considered, FGM1 (blue dot) and FGM2 (red dot) data are the same as in Fig. 1
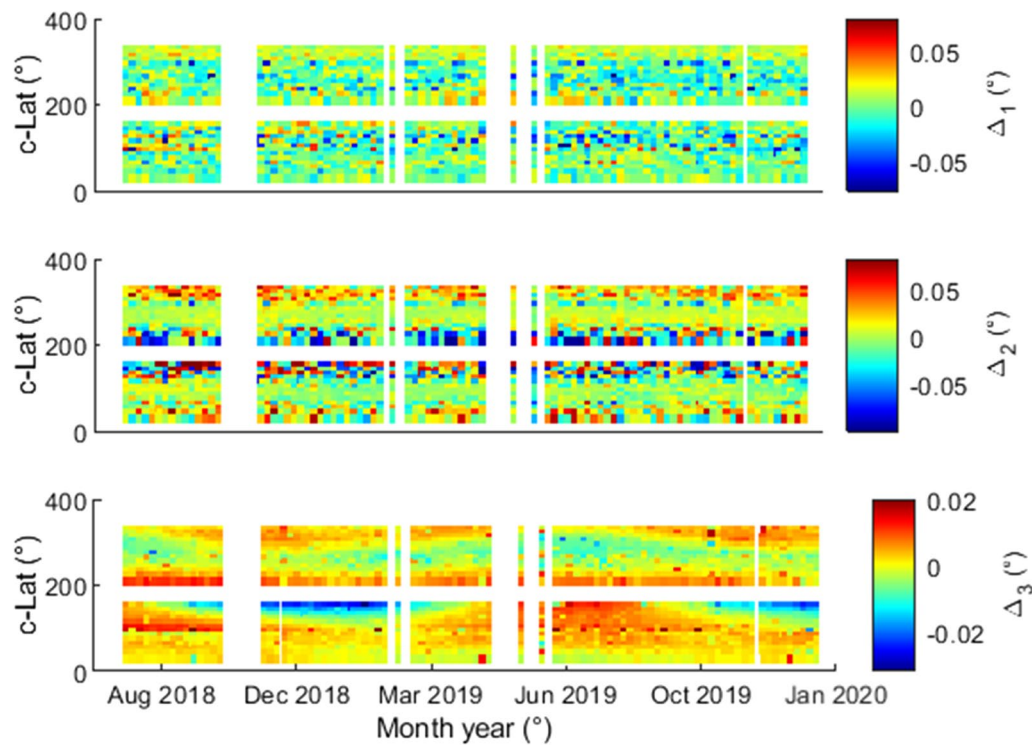
Fig. 5 Spatial and temporal variations of the non-orthogonal angles from August 1st, 2018 to December 31st, 2019

variations, but also varies with the geographical longitude (*Lon*) and latitude ($c-Lat$). In addition, the sensor temperature of FGM itself can reflect the changes of heat flux from the space to a certain extent.

The correlations between the above five factors and Δ are measured by the Maximal Information Coefficient (MIC) (Reshef et al. 2011). MIC gives statistically independent variables a score that tend to zero, and it assigns scores that tend to one to both, the nonlinear and linear relations. Therefore, it helps to uncover nonlinear relationships. Table 1 shows the MIC scores between $Az, El, c-Lat, Lon, Te_{FGM2}$ (the sensor temperature of FGM2) and Δ of FGM2, resulting from analysis of total twelve periods data used in Fig. 1. MIC gives high scores to four factors except *Lon*, with scores over 0.9 between Δ and $Az, El, c-Lat$, respectively, and 0.86 between Δ and Te_{FGM2}. There are also distinct correlations between $c-Lat$ and Az, El and Te_{FGM2}, which means these four factors are not independent. The correlations between latitude and the two solar incident angles and probe temperature are 0.9801, 0.7044, and 0.5658, respectively. In comparison with the correlations between the other two factors, latitude to some extent is the most important of the four factors. Considering such high correlation, we take latitude into

modeling. In addition, it is found that the inclusion of latitude can achieve better effects. Moreover, the variation of non-orthogonal angles is fairly correlated with sensor temperature, but not as high as other factors, because the sensor temperature only reflects a single point of temperature in the sensor. Due to non-ideal thermal insulation of FGM, the variation of the heat-flow can cause the variation of the thermal distribution in the sensor, result in the variation of the sensor orthogonality.

The high correlation between external heat flow related factors and Δ explains the similarity in Fig. 6, where the solar illumination, the sensor temperature of FGM and geographic latitude of CSES are approximately the same after a 1-year interval. Highly similar $Az, El, c-Lat, Te_{FGM2}$ will result in similar variations in the non-orthogonal angles of FGM. Therefore, as it is shown in Eq. (10), a four-dimensional *N*th order Taylor polynomial model (T model) is established to approximate the relations between $Az, El, c-Lat, Te_{FGM2}$ and Δ. The Taylor coefficient is solved by the LS algorithm (Chatterjee and Hadi 1986) and is calculated according to the Δ shown in Fig. 5 based on data in year 2019 only, and then we test the applicability of the model in other years:

Tong *et al. Earth, Planets and Space*   (2023) 75:21
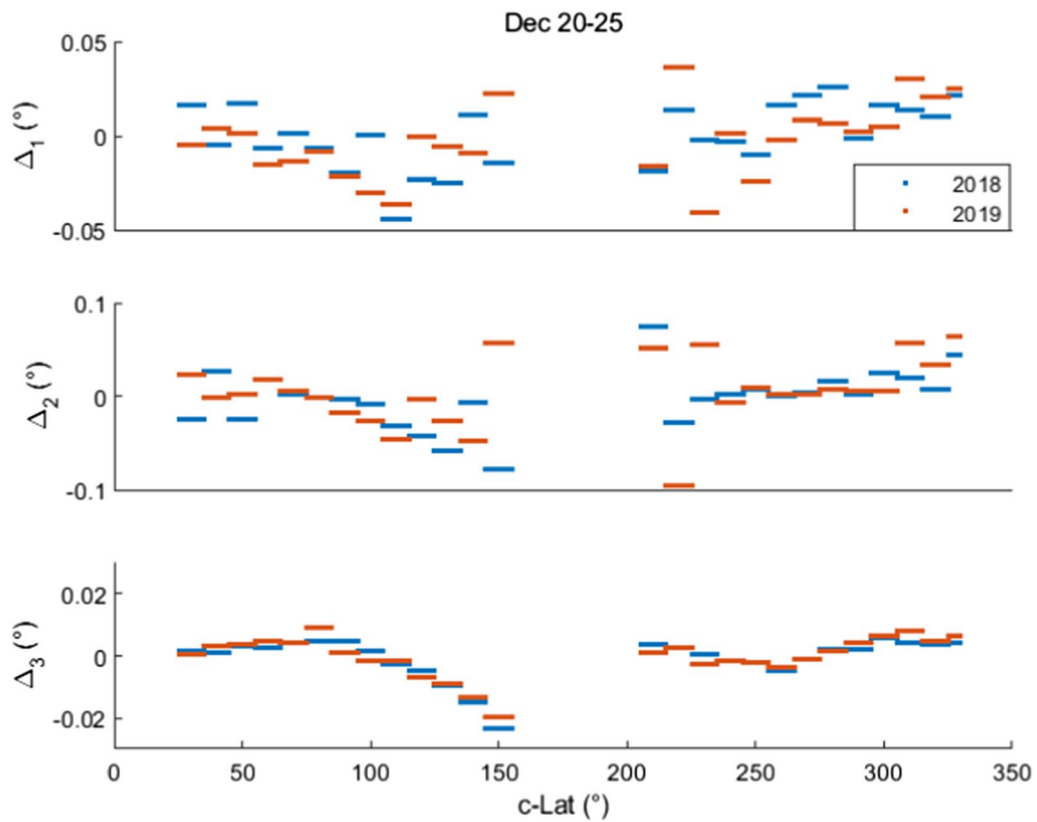
Page 8 of 15

Fig. 6 In-orbit inversion of orbital variation of the non-orthogonal angles on December 20–25, data from year 2018 are shown as blue dots and that from year 2019 are shown as red dots;
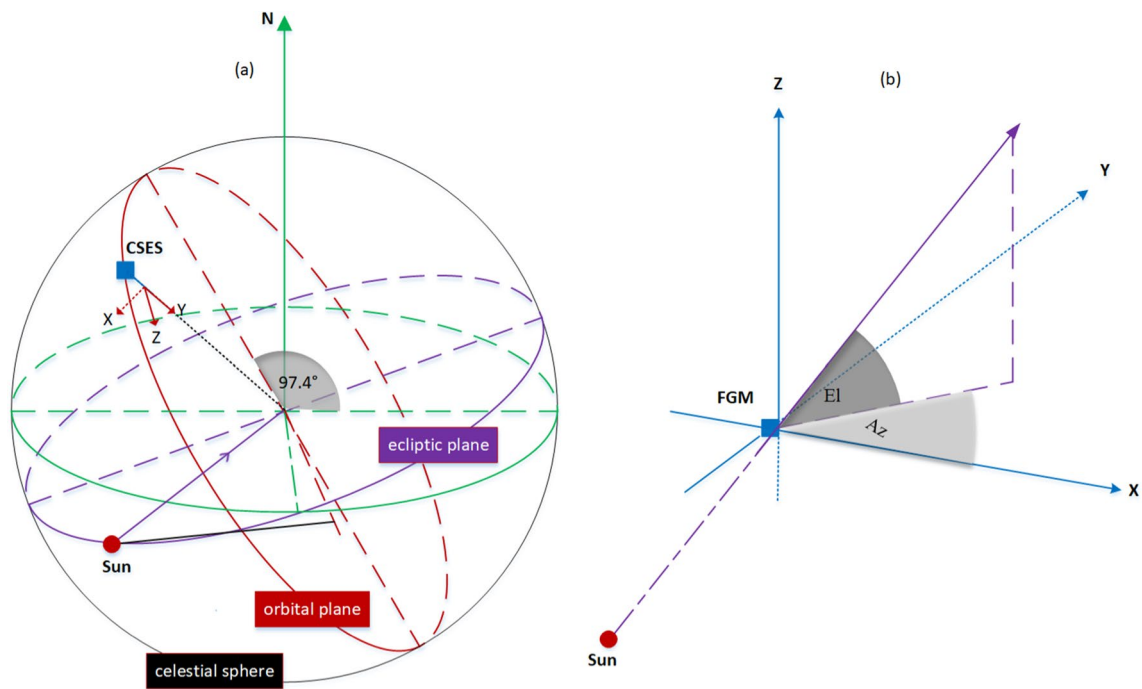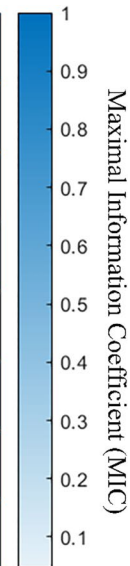

Fig. 7 Schematic diagram of CSES orbit (left); azimuth and elevation of the solar illumination vector in the FGM sensor coordinate system (right);

Table 1 Correlations between $Az, El, c-Lat, Lon, Te_{FGM2}$ and FGM2 Δ, evaluated based on MIC

	c-Lat	Lon	Az	El	Te_FGM2
Δ_1	0.995	0.0495	0.9825	0.9451	0.8645
Δ_2	0.9949	0.0447	0.9825	0.9398	0.8592
Δ_3	0.995	0.0461	0.9763	0.9451	0.8645
c-Lat	1	0.0658	0.9801	0.7044	0.5658
Lon	0.0658	1	0.0506	0.0457	0.0527
Az	0.9801	0.0506	1	0.475	0.4115
El	0.7044	0.0457	0.475	1	0.5892
Te_FGM2	0.5658	0.0527	0.4115	0.5892	1

Maximal Information Coefficient (MIC)

$$\Delta \Leftarrow F = \begin{cases} \displaystyle\sum_{k_1=1}^{N}\sum_{k_2=1}^{N}\sum_{k_3=1}^{N}\sum_{k_4=1}^{N} A^0_{k_1 k_2 k_3 k_4} c\text{-}Lat^{k_1-1} Az^{k_2-1} El^{k_3-1} Te^{k_4-1}, nightside \\ \displaystyle\sum_{k_1=1}^{N}\sum_{k_2=1}^{N}\sum_{k_3=1}^{N}\sum_{k_4=1}^{N} A^1_{k_1 k_2 k_3 k_4} c\text{-}Lat^{k_1-1} Az^{k_2-1} El^{k_3-1} Te^{k_4-1}, dayside \end{cases},$$

(10)

The model is expanded at zero, where the Taylor coefficient of three non-orthogonal angles is $A^{0,1}_{k_1 k_2 k_3 k_4}$, and the dayside and nightside both have $3 * N^4$ coefficients. With a truncation order $N = 3$, the T model is fitted to characterize the annual variation of non-orthogonal angles. The trends in scalar residuals are effectively eliminated, and the calibration results of scalar residuals based on T model are similar to those shown in Fig. 4. Figure 8a shows the variation of non-orthogonal angles calculated by T model based on $Az, El, c-Lat, Te_{FGM2}$ factors throughout year 2019, where the left plot shows in Az, El and Te_{FGM2} coordinates, and the right plot of shows in $Az, c-Lat,$ and Te_{FGM2} coordinates. The three non-orthogonal angles smoothly vary in-orbit under the influence of the four factors. Figure 8b shows how the non-orthogonal angles vary with the most important factor (co-latitude) in year 2019.

CSES data calibration with T model

CSES has been operating continuously over 4 years, enabling us to study the long-term behavior of the vector magnetometer in orbit. Therefore, the T model trained by the magnetic field data in 2019, is utilized to calibrate the currently available magnetic field data (August 2018 to May 2021). Take FGM2 as an example and update its 9 instrument parameters (three gain factors, three offsets, and three non-orthogonal angles) every 5 days. Figure 9 shows the T model calibration results of instrument parameters of FGM2. The instrument parameters show a smooth trend via time, compatible with expectation. Figures 10 plots the difference of FGM2 instrument parameters before and after using T model, respectively. The results of 9 parameters are labeled with bu/au, before/after calibration, respectively. The difference shows a trend of annual variation, because the instrument parameters before calibration are distorted when without considering the thermal drift of non-orthogonal angles. The gain of the *x*-component sensor of FGM shown in Figs. 9 and 10 has an order of magnitude difference compared to the other components. This may be due to the fact that as previously mentioned the *x*-component of the sensor measures weaker geomagnetic field, and might have larger errors in its parameters even after T model calibration.

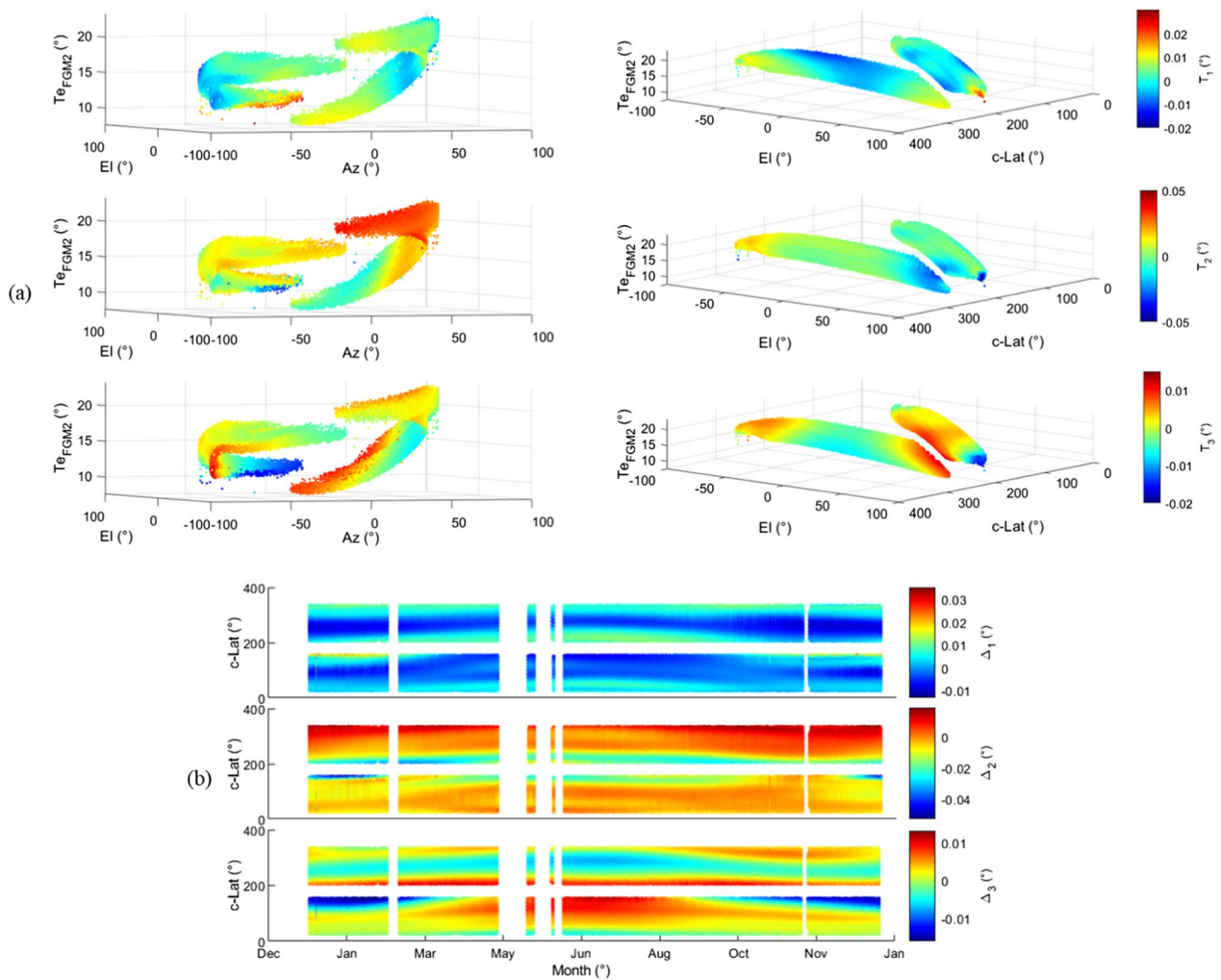Tong *et al. Earth, Planets and Space*   (2023) 75:21

Page 10 of 15

Fig. 8 The variation of three non-orthogonal angles of FGM2 calculated by T model in the year of 2019

The left and right column in Fig. 11 shows the probability distributions of the scalar residuals before and after using T model, respectively, for eight latitude zones in February 2021. In a normal probability plot, the plot will be linear if the data are normally distributed (Tøffner-Clausen et al. 2016), so the multiple dashed lines (the reference lines) in Fig. 11 is used to assess the degree of normality of the scalar residuals. Comparing the plot of the scalar residuals to their reference lines, it is clearly seen that the residual distributions shift from non-normality to normality, and the distributions in different latitude zones are more consistent with each other after using T model. Figure 12 shows the temporal variation of scalar residuals of FGM1 and FGM2 in February 2021. Compared with the linearly calibrated data (blue error bar), the variance of scalar residuals decreases significantly after using T model (red error bar), indicating that

scalar residuals in different temporal and latitude zones have been well-calibrated.

Figure 13 compares the distributions of scalar residuals of data, between August 2018 and May 2021 before (blue) and after (red) using T model. The histograms indicate the probability density distributions and the solid lines represent the normal distributions. There are two peaks in the residual histogram before using T model, and particularly the histogram of FGM1 clearly reflects difference caused by day–night variations of non-orthogonal angles. In addition, the scalar residuals of FGM1 are slightly larger than that of FGM2, because the FGM1 sensor is closer to the spacecraft and more vulnerable to satellite interferences. The scalar residuals of FGM1 and FGM2 approximately obey the normal distribution of N1,bu(-0.0288,1.14022^2), and N2,bu(− 0.0192,0.9484^2), respectively. After using

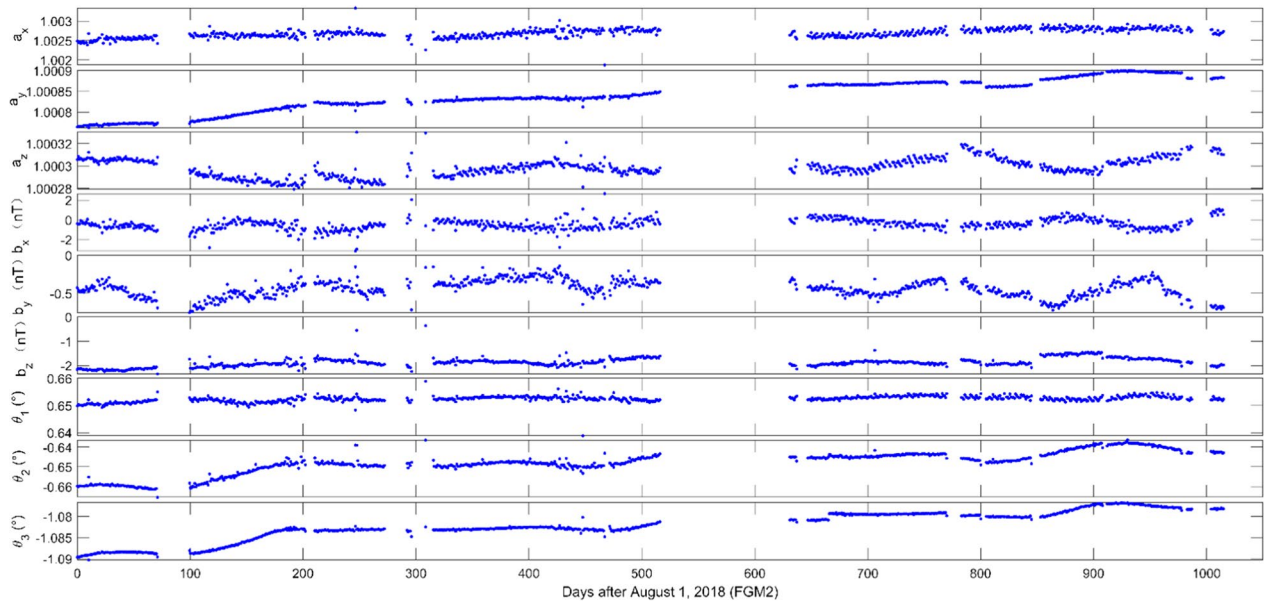Tong *et al. Earth, Planets and Space*   (2023) 75:21

Page 11 of 15

Fig. 9 Instrument parameters from August 1st, 2018 to May 30th, 2021, estimated after the application of T model
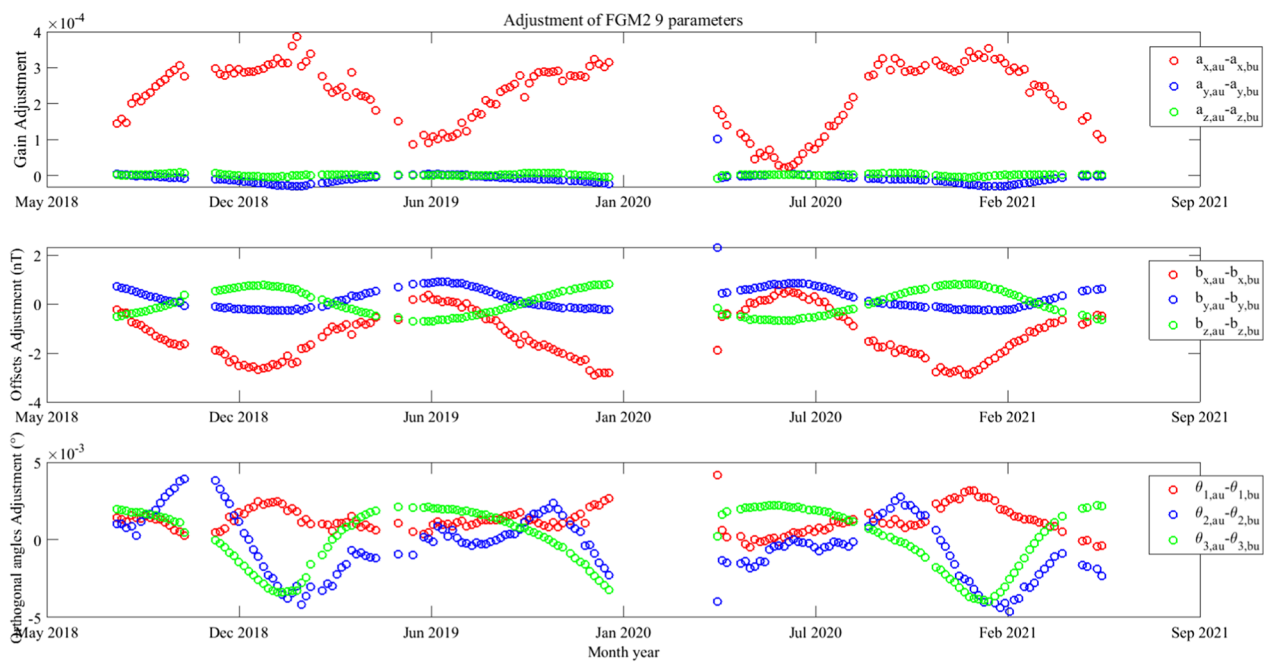

Fig. 10 Adjustment of FGM2 linear parameters, including the gain factors, offsets, and orthogonal angles from August 1th, 2018 to May 30th, 2021

T model, the scalar residuals of FGM1 approximately obey the normal distribution of N1,au(−0.0220,0.6491²), and those of FGM2 approximately obey the normal distribution of N2,au(−0.0236,0.4850²). The mean values of scalar residuals rarely change, but σ decreases significantly. Calibration results show that T model correctly reflects both orbital variation and annual variation in non-orthogonal angles with the solar illumination angle, geographic latitude, and sensor temperature. Furthermore, the model seems robust, that it works equally well on the magnetic field data of 2018, 2020, and 2021, reduces the scalar residuals, and greatly eliminates the trends in scalar residuals.
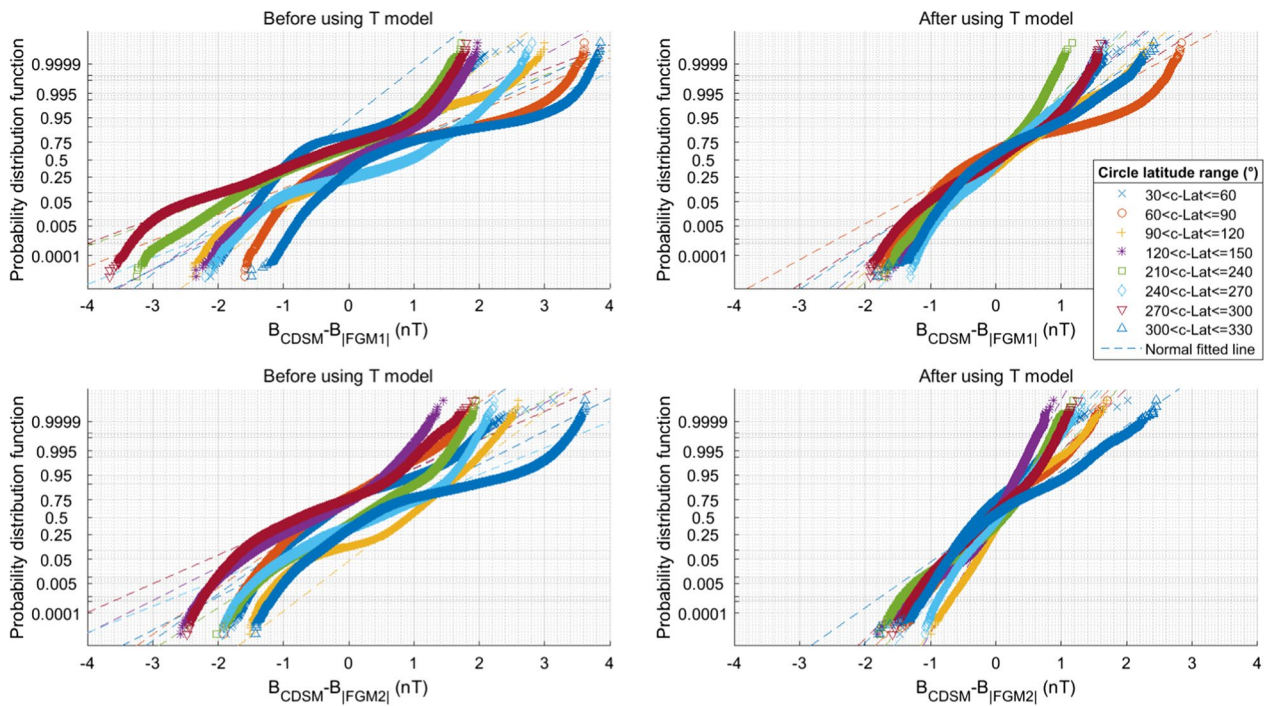
Fig. 11 The normal probability of scalar residuals for eight latitude zones in February 2021. The left/right plots show residuals before/after using T model. The top/bottom plots show residuals of FGM1/FGM2
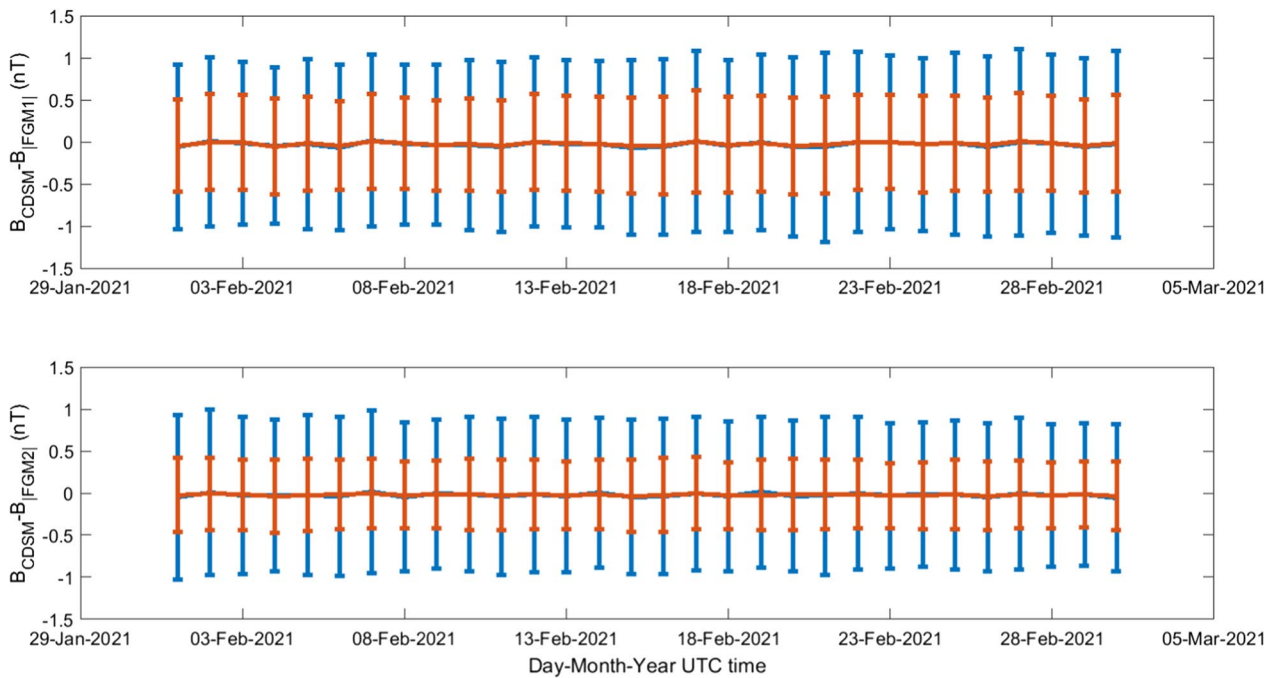

Fig. 12 The temporal variation of scalar residuals of FGM1 and FGM2 in February 2021, before using T model (blue error bar), after using T model (red error bar)
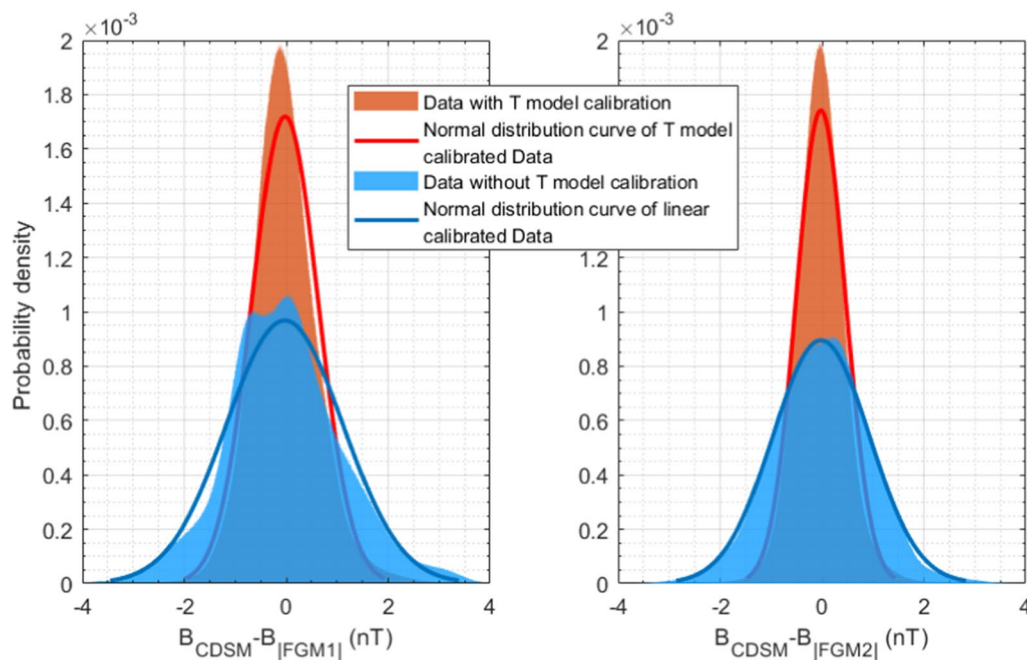
Tong *et al. Earth, Planets and Space* (2023) 75:21

Page 13 of 15

Fig. 13 Probability density histogram of scalar residuals of nearly 3 year FGM data (August 2018 to May 2021)

Conclusions and discussion

There are three basic conditions for application of the scalar equation to calibrate vector magnetic field data in orbit: first, the linear parameters of vector magnetic field sensor are stable; second, the scalar magnetometer data is accurate; third, the magnetic field measurements by vector sensor and scalar sensor are synchronized. When the basic conditions are not met, the calibration method needs to be adjusted according to the instrument behaviors. The trends in the scalar residuals maybe caused by the variation of the gains, offsets or non-orthogonal angles during the orbit. However, if it were gain or offset, the calibration result would deviate severely from the instrument characteristics. For example, when assuming the gains change during the orbit, the dependence of the gains on the temperature would be approx. 200 ppm/°C, 10 times the ground value (20~30 ppm/°C, Cheng et al. 2018). Since the gains relate the thermal expansion coefficients of the coil and is relatively stable. This unpractically large coefficient implies the gains are not the cause. In addition, the offsets are ruled out for the same reason. Meanwhile, the influence analysis of orthogonality on scalar residuals shows that the main cause of the trends in scalar residuals is the orthogonality variations.

The MIC correlation analysis helps to find out that the orthogonality variations are related to space thermal conditions. It's worth noting that the deformation occurs by the thermal gradient in the sensor; therefore, the orthogonality variations have higher correlation with the sun-illumination angle, latitude than the sensor temperature. Based on those relevant factors and the HPM data in 2019, we establish a multi-dimensional polynomial model for FGM, and name it as T model.

After adopting T model, the scalar residuals of the vector magnetic field data drop to about 0.5 nT. The remaining scalar residuals may partly owe to the nonlinearity of the magnetometer. Compared with the calibration results (Zhou et al. 2019) at the initial stage of the mission, this paper processes the dayside and nightside magnetic field data together and gets one set of offsets and gains for the full orbit which is a more reliable and reasonable way in response to the operational status of FGM. The annual variation of linear parameters of FGM sensors vanished after calibration with T model, and the scalar residuals are optimized in general and tend to be more random in different revisiting cycles and latitudinal zones. We confirm the validity of data calibration results, through reasonable explanations of the linear parameters, and further data analysis, such as normal distribution of scalar residuals.

The validation shows that T model is effective in CSES's current in-orbit status. The new algorithm is going to be included in routine processing of the HPM data to improve the quality of vector magnetic field data.

Tong *et al. Earth, Planets and Space*   (2023) 75:21

Page 14 of 15

Supplementary Information

The online version contains supplementary material available at https://doi.org/10.1186/s40623-023-01766-y.

Additional file1: Author Affiliations Amendment.

Author contributions

YT and BZ carried out the calibration. YT drafted the manuscript. LL, BC and YZ contributed to the development of methodology. WM, RL, and AP have contributed to the analysis of CDSM data. YY, ZZ and XS have contributed to the HPM data analysis. All authors revised and approved the final manuscript. All authors read and approved the final manuscript.

Availability of data and materials

The CSES data sets analyzed during the current study are available in the repository of National Institute of Natural Hazards, Ministry of Emergency Management of China.

Declarations

Competing interests

The authors declare that they have no competing interests.

Author details

[1]State Key Laboratory of Space Weather, National Space Science Center, Chinese Academy of Sciences, Beijing 100190, China. [2]Key Laboratory of Solar Activity and Space Weather, National Space Science Center, Chinese Academy of Sciences, Beijing 100190, China. [3]School of Astronomy and Space Science, University of Chinese Academy of Sciences, Beijing 100049, China. [4]Space Research Institute, Austrian Academy of Sciences, Graz 8042, Austria. [5]Institute of Experimental Physics, Graz University of Technology, Graz 8010, Austria. [6]National Institute of Natural Hazards, Ministry of Emergency Management of China, Beijing 100085, China.

References

Chatterjee S, Hadi A (1986) Influential observations, high leverage points, and outliers in linear regression. Stat Sci. https://doi.org/10.1214/ss/1177013622

Cheng B, Zhou B, Magnes W, Lammegger R, Pollinger A (2018) High precision magnetometer for geomagnetic exploration onboard of the China seismo-electromagnetic satellite. Sci China Technol Sci 61(5):659

Friis-Christensen E, Lühr H, Hulot G (2006) Swarm: a constellation to study the earth's magnetic field. Earth Planets Space 58(4):351–358. https://doi.org/10.1186/BF03351933

Kennedy J (2011) Particle swarm optimization. Proc IEEE Int Conf Neural Netw 4(8):1942

Langel R, Ousley G, Berbert J, Murphy J, Settle M (1982) The MAGSAT mission. Geophys Res Lett 9(4):243

Mezura-Montes E, Coello C (2011) Constraint-handling in nature-inspired numerical optimization: past, present and future. Swarm Evol Comput 1(4):173–194

Olsen N, Clausen LT, Sabaka TJ, Brauer P, Merayo JMG, Jørgensen JL, Léger J-M, Nielsen OV, Primdahl F, Risbo T (2003) Calibration of the Ørsted vector magnetometer. Earth Planets Space 55(1):11

Pedersen, M. (2010). Good Parameters for Particle Swarm Optimization,Tech. rep, Hvass Laboratories. https://doi.org/10.13140/RG.2.2.23771.49445

Pollinger A, Amtmann C, Betzler A, Cheng B, Ellmeier M, Hagen C, Jernej I, Lammegger R, Zhou B, Magnes W (2020) In-orbit results of the coupled dark state magnetometer aboard the China Seismo-electromagnetic satellite. Geosci Instrum Method Data Syst 9:275–291. https://doi.org/10.5194/gi-9-275-2020

Primdahl F, Risbo T, Merayo JMG, BrauerTFfner-Clausen PL (2006) In-flight spacecraft magnetic field monitoring using scalar/vector gradiometry. Meas Sci Technol 17(6):1563

Qi X, XiaoLei G, JinGang C, LiFei M, Na LI, YanJing Z (2018) Calibration methods of the interference magnetic field for low earth orbit (LEO) magnetic satellite. Chin J Geophys 61(8):3134–3138. https://doi.org/10.6038/cjg2018L0408

Reshef D, Reshef Y, Finucane H, Grossman S, McVean G, Turnbaugh P, Lander E, Mitzenmacher M, Sabeti P (2011) Detecting novel associations in large data sets. Science 334:1518–1524. https://doi.org/10.1126/science.1205438

Rother M, Choi S, Mai W, Lüuhr H, Cooke D (2005) Status of the CHAMP ME data processing. In: Reigber C, Lühr H, Schwintzer P, Wickert J (eds) Earth Observation with CHAMP: Results from Three Years in Orbit. Springer, Berlin

Shen X, Zhang X, Yuan S, Wang L, Cao J, Huang J, Zhu X, Piergiorgio P, Dai J (2018) The state-of-the-art of the China seismo-electromagnetic satellite mission. Sci China Technol Sci 61(5):634

Tøffner-Clausen L, Lesur V, Olsen N, Finlay CC (2016) In-flight scalar calibration and characterisation of the Swarm magnetometry package. Earth Planets Space 68(1):129. https://doi.org/10.1186/s40623-016-0501-6

Tong Y, Cheng B, Miao Y, Zhou B, Zhu X, Yang Y, Liu J, Gou X, Zhang Y, Wang J, Li L, Magnes W, Lammegger R, Pollinger A, Zeren Z, Shen X (2021) Analysis and elimination of tri-band beacon interference with the fluxgate sensors onboard CSES. Science China Technol Sci 64(10):2328–2336. https://doi.org/10.1007/s11431-020-1799-1

Wang J, Shen X, Yang Y, Zhima Z, Hulot G, Olsen N, Zhou B, Magnes W, De Santis A, Huang J, Guo F, Liu W, Yu J (2021) Initial scalar lithospheric magnetic anomaly map of China and surrounding regions derived from CSES satellite data. Sci China Technol Sci. https://doi.org/10.1007/s11431-020-1727-0

Yang Y, Hulot G, Vigneron P, Shen X, Zhima Z, Zhou B, Magnes W, Olsen N, Tøffner-Clausen L, Huang J, Zhang X, Yuan S, Wang L, Cheng B, Pollinger A, Lammegger R, Dai J, Lin J, Guo F, Yu J, Wang J, Wu Y, Zhao X, Zhu X (2021a) The CSES global geomagnetic field model (CGGM): an IGRF-type global geomagnetic field model based on data from the China Seismo-Electromagnetic Satellite. Earth, Planets and Space 73(1):45. https://doi.org/10.1186/s40623-020-01316-w

Yang Y, Zhou B, Hulot G, Olsen N, Wu Y, Xiong C, Stolle C, Zhima Z, Huang J, Zhu X, Pollinger A, Cheng B, Magnes W, Zhao X, Shen X (2021b) CSES High precision magnetometer data products and example study of an intense geomagnetic storm. J Geophys Res Space Phys. https://doi.org/10.1029/2020JA028026

Yin F, Lühr H (2011) Recalibration of the CHAMP satellite magnetic field measurements. Measurement Sci and Technol 22:055101. https://doi.org/10.1088/0957-0233/22/5/055101

Zhang J, Cheng B, Tong Y, Miao Y, Zhou B, Pollinger A, Zhu X, Yang Y, Gou X, Zhang Y, Wang J, Li L, Magnes W, Lammegger R (2022) Comparison of scalar magnetic field data of China seismo-electromagnetic satellite and swarm satellites front. Earth Sci 10:866438. https://doi.org/10.3389/feart.2022.866438

Zhima Z, Zhou B, Zhao S, Wang Q, Huang J, Zeng L, Lei J, Chen Y, Li C, Yang D et al (2022) Cross-calibration on the electromagnetic field detection

payloads of the China seismo-electromagnetic satellite. SCIENCE CHINA Technol Sci. https://doi.org/10.1007/s11431-021-1965-2

Zhou B, Yang Y, Zhang Y, Gou X, Cheng B, Wang J, Li L (2018) Magnetic field data processing methods of the China seismo-electromagnetic satellite. Earth Planet Phys 2(455):461. https://doi.org/10.6464/epp2018043

Zhou B, Cheng B, Gou X, Li L, Zhang Y, Wang J, Magnes W, Lammegger R, Pollinger A, Ellmeier M, Xiao Q, Zhu X, Yuan S, Yang Y, Shen X (2019) First in-orbit results of the vector magnetic field measurement of the High Precision Magnetometer onboard the China seismo-electromagnetic satellite. Earth Planets Space 71(1):20

Publisher's Note